# Synthesis, Characterization, and Crystal Structure of *N*-(3-nitrophenyl)cinnamamide

**Jung-Seop Lee [1], Matthias Zeller [2], Shrikant Dashrath Warkad [1] and Satish Balasaheb Nimse [1,*]**

[1] Institute of Applied Chemistry and Department of Chemistry, Hallym University, Chuncheon 200-702, Korea; wndtjq93@hanmail.net (J.-S.L.); shrikant.warkad@hallym.ac.kr (S.D.W.)
[2] Department of Chemistry, Purdue University, West Lafayette, IN 47907, USA; zeller4@purdue.edu
[*] Correspondence: satish_nimse@hallym.ac.kr; Tel.: +82-33-248-2076

**Abstract:** *N*-(3-nitrophenyl)cinnamamide **1** with formula $C_{15}H_{12}N_2O_3$ was synthesized, and its crystal structure was determined by single-crystal X-ray diffraction analysis. Compound **1** crystallizes in the monoclinic space group P21/n with unit cell dimensions: a = 6.7810 (5) Å, b = 23.0913 (15) Å, c = 8.2079 (5) Å, V = 1282.76 (15) Å$^3$, Z = 4, determined at 150 K with MoK$\alpha$ radiation. The experimental structure refined against atomic scattering factors is compared with the structure obtained using a Hirshfeld Atom Refinement (HAR) approach and Density Functional Theory (DFT) geometry optimizations.

## 1. Introduction

Life-threatening infections caused by multidrug-resistant Gram-positive and Gram-negative bacteria are rising at an alarming level in many countries around the world [1,2]. Due to the occurrence in plants and its low toxicity, cinnamic acid has been evaluated as an antioxidant and also, as an active antimicrobial compound [3,4]. Some cinnamic acid derivatives are reported to demonstrate a superior antimicrobial activity to that of cinnamic acid itself [5,6]. Pharmaceutical active ingredients containing the nitro group in their structure constitute a vast family with diverse pharmacological effects [7]. In aromatic compounds, a nitro group has a strong electron-withdrawing effect on the aromatic π-system, resulting in deactivation of the ring towards electrophilic aromatic substitutions [8]. The presence of the nitro group has also been reported to be responsible for the toxicity of certain drugs [9]. In a previous study, we have reported that the *m*-nitro substituent can endow cinnamamide derivatives with a potent antibacterial activity as compared to the *o*-nitro and *p*-nitro substituents [10].

Herein, we report the synthesis and characterization of *N*-(3-nitrophenyl)cinnamamide by various spectroscopic techniques. A combination of single-crystal X-ray diffraction and density functional theory (DFT) simulations were used for structure elucidation and description of the electronic properties of the compound.

## 2. Materials and Methods

### 2.1. Synthesis and Characterization

All chemicals and solvents required for synthesis and characterization were purchased from commercial sources. The final product was characterized by $^1$H and $^{13}$C NMR on a Jeol FT-NMR spectrometer (400 MHz; JEOL, Japan). The chemical shifts (δ) are reported in parts per million (ppm) relative to TMS, and the coupling constants (J) are quoted in Hz. UV absorptions and fluorescence emission spectra were measured on the Shimadzu UV-1800 spectrometer (Shimadzu, Japan) and Agilent Cary Eclipse Fluorescence Spectrophotometer, respectively. Mass spectra were recorded on an

Agilent-5977E spectrometer (Agilent Technologies, USA). High-resolution mass spectra were obtained on a JMS-700 Mass Spectrometer (JEOL, Japan).

## 2.2. X-Ray Diffraction

The X-ray analysis was performed using a Bruker AXS D8 Quest CMOS diffractometer (Bruker, USA). A suitable single crystal was carefully selected under an optical microscope and was mounted with the help of a trace of Fomblin oil on a Mitegen micromesh mount. Then, it was transferred to the goniometer head with a fixed chi angle, a molybdenum K$\alpha$ wavelength fine focus sealed X-ray tube ($\lambda = 0.71073$), a single crystal curved graphite incident beam monochromator, a Photon100 CMOS area detector, and an Oxford Cryosystems low-temperature device. X-ray diffraction data were collected at 150 K using $\omega$ and $\varphi$ scans to a maximum resolution of $\Theta = 33.172°$ (0.65 Å). Data reduction, scaling, and absorption corrections were performed using SAINT (Bruker, V8.38A). The final completeness is 99.00% out to 33.172° in $\Theta$. Multi-scan absorption correction was performed using SADABS 2016/2 [11,12]. The absorption coefficient $\mu$ of this material is 0.099 mm$^{-1}$ at this wavelength ($\lambda = 0.71073$ Å), and the minimum and maximum transmissions were 0.674 and 0.747.

The space group was determined based on systematic absences using XPREP [13] as P2$_1$/n (# 14). The structure was solved using direct methods with ShelXS-97 [14] and refined by full-matrix least-squares on F$^2$ using ShelXL-2018/3 [15] and the graphical interface ShelXLE (Rev937) [16]. All non-hydrogen atoms were refined anisotropically. Hydrogen atom positions were calculated geometrically and improved using a riding model. C–H bond distances were constrained to 0.95 Å for aromatic and alkene C–H moieties. The N–H bond distance of the amide N–H group was constrained to 0.88 Å. U$_{iso}$(H) values were set to 1.2 times U$_{eq}$(C/N). Olex2 [17], Mercury [18] and Platon [19] were used for molecular measurements. Mercury, Olex2, PyMol [20], and POVRay [21] were used for molecular visualization.

## 2.3. Computational Studies

Hirshfeld Atom Refinement (HAR) with Olex2 [12] was performed using the "Restricted Hartree–Fock" method with a def2-SVP basis set [22,23]. Density functional theory (DFT) calculations were carried out using Gaussian 09 [24]. The molecular geometries of the singlet ground state of Compound **1** were optimized in the gas phase at the DFT level using hybrid B3LYP functions with a 6-31G++(d,p) basis set [25,26]. A frequency calculation was carried out to ensure the optimized molecular structure corresponds to a local minimum [19]. Avogadro 1.2.0 [27] was used to obtain the HOMO, LUMO results, and information for bond length and bond angles.

## 3. Results and Discussion

### 3.1. Synthesis and Characterization

Six reports of the synthesis of (*N*-(3-nitrophenyl)cinnamamide **1** have been published between 1963 and 2015 [10,28–32]. However, no crystallography data had been reported to date (Cambridge Structural Database, October 2019). The synthesis employed here is a modification of that reported by Wang et al. [33]. Cinnamoyl chloride (4.10 g, 25 mmol), pre-dissolved in 5 mL diethyl ether, was added dropwise to a 30 mL stirred solution of 3-nitroaniline (4.15 g, 30 mmol) in diethyl ether at 0 °C. The mixture was stirred at 0 °C for 30 min and then at RT for 3 hours. Upon completion of the reaction, the solvent was evaporated, and then 100 mL of dichloromethane was added to the flask. The solution was washed with 1N HCl (3x) and with 1N NaHCO$_3$ (2x). The organic layer was dried over Mg$_2$SO$_4$, filtered, and then the solvent was evaporated completely to obtain the target material (4.95 g, 18.5 mmol, 74.0%) (Scheme 1). Yellow crystals suitable for X-ray diffraction of Compound **1** were obtained by slow evaporation from ethyl acetate. The $^1$H NMR and $^{13}$C NMR were recorded (Supplementary Materials Figure S1 and Figure S2). $^1$H NMR (d$_6$-DMSO, 400 MHz, 298 K) (assignments labelled as in Figure 1): $\delta$ (ppm) 10.73 (br, 1H, -NH), 8.76 (1H, t, Ar-H, B2), 8.00 (d, 1H, *J* = 8.14Hz, Ar-H,

B4), 7.94 (d, 1H, *J* = 8.22Hz, Ar-H, B6), 7.46–7.67 (m, 7H, Ar-H, CH=CH, B6 and A2-A6), 6.83 (d, 1H, *J* = 15.79 Hz, CH=CH, 2-3). $^{13}$C NMR (d6-DMSO): δ (ppm) 164.18 (C=O), 148.05 (NO$_2$-Ar-C), 141.31 (Ar-CH=CH), 140.40, 134.46, 130.32, 130.14, 129.12, 127.94, 125.21, 117.91, 113.33 (Ar), 121.49 (CH=CH-C=O). JEOL JMS 700, EI$^+$ mode: m/z = 268.0847 [M]$^+$ (Supplementary Materials Figure S3). Compound **1** (100 nM – 25 μM) demonstrated the absorption maximum (λ$_{max}$) at 296nm in the DMSO solution (Supplementary Materials Figure S4). However, measurable fluorescence emission was not observed in the entire concentration range.
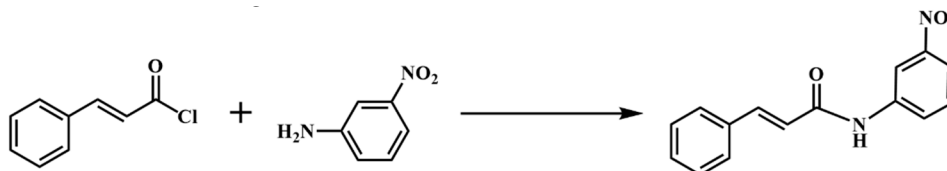


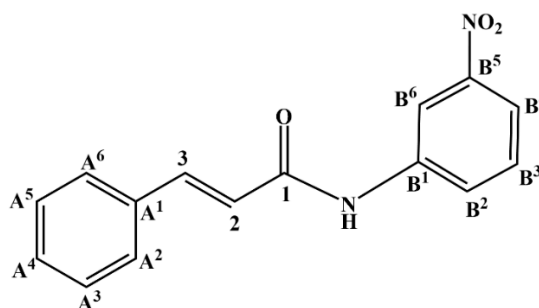**Scheme 1.** Synthesis of *N*-(3-nitrophenyl)cinnamamide (Compound **1**).



**Figure 1.** Ring nomenclature (A and B rings).

### 3.2. X-Ray Diffraction

The single-crystal diffraction data are summarized in Table 1. An ORTEP diagram of Compound **1** is presented in Figure 2. Bond distances and angles in Compound **1** are unusual and as expected. The molecule consists of several planar segments that are close to co-planar with each other, leading to a nearly planar molecule.

The angle between the planes of the A ring and nitro-substituted B ring of compound **1** is 6.66 (3)°. The torsion angles between the propene amide bridge and the A and B rings are −1.32 (10)° (C2–C3–C4–C9), −2.1 (9)° (C1–C2–C3–C4), −9.82 (9)° (C1–N1–C10–C11), and −2.64 (8)° (C2–C1–N1–C10) resulting in a close to planar molecule. The conformation of the double bond and the amide unit is all *trans*, leading to an extended "linear" structure. This conformation is in part stabilized by an internal C–H···O interaction, between H15 of the nitrophenyl ring and the amide oxygen atom O1, with an H···O of 2.27 Å. The short C15···O1 distance of 2.8623 (10) Å indicates this interaction to be stabilizing, despite of the less than favorable C–H···O angle of 119.6°.
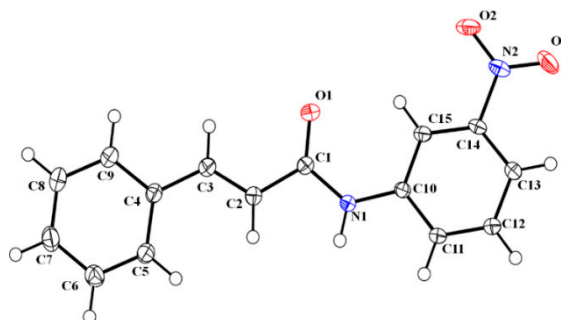


**Figure 2.** ORTEP view of Compound **1**, showing 50% probability displacement ellipsoids and atom labeling.

Packing of molecules in the solid-state is governed by the close to planar and extended conformation, leading to ribbons of parallel sheets of molecules that are stacked through $\pi\cdots\pi$ stacking interactions. Within each ribbon, molecules are connected through a series of N-H$\cdots$O and C-H$\cdots$O interactions of various strengths (Table 2).

**Table 1.** Summary of crystal data.

| Formula | $C_{15}H_{12}N_2O_3$ |
|---|---|
| Formula mass (g/mol) | 268.27 |
| Crystal system | Monoclinic |
| Space group | $P2_1/n$ |
| a, b, c (Å) | 6.7810 (5), 23.0913 (15), 8.2079 (5) |
| $\alpha$, $\beta$, $\gamma$ (°) | 90, 93.538(3), 90 |
| V (Å$^3$); Z | 1282.76 (15); 4 |
| Temperature (K) | 150 |
| Radiation type | MoK$\alpha$ ($\lambda$ = 0.71073) |
| $\mu$(Mo K$\alpha$), mm | 0.10 |
| Collected reflections | 20955 |
| 2$\Theta$ range (°) | 2.638, 33.172 |
| Unique reflections | 4759 |
| $R_{int}$ | 0.031 |
| $R_{sigma}$ | 0.0224 |
| $R_1$ [I$\geq$2$\sigma$ (I)] | 0.0442 |
| $wR_2$ | 0.122 |
| F(000) | 560.0 |
| Crystal size (mm) | 0.55 × 0.45 × 0.19 |
| Crystal description | Clear, yellow |

**Table 2.** Selected hydrogen-bond parameters (Å, °).

| *D*—H$\cdots$*A* | *D*—H (Å) | H$\cdots$*A* (Å) | *D*$\cdots$*A* (Å) | *D*—H$\cdots$*A* (°) |
|---|---|---|---|---|
| C2—H2$\cdots$O2$^i$ | 0.95 | 2.38 | 3.2534 (10) | 152.1 |
| C11—H11$\cdots$O3$^i$ | 0.95 | 2.42 | 3.3490 (11) | 165.6 |
| C15—H15$\cdots$O1 | 0.95 | 2.27 | 2.8623 (10) | 119.6 |
| N1—H1$\cdots$O2$^i$ | 0.88 | 2.33 | 3.1895 (9) | 164.7 |
| C2—H2$\cdots$O2$^i$ | 0.95 | 2.38 | 3.2534 (10) | 152.1 |

Symmetry code(s): (i) x, y, z − 1.

The strongest of these interactions is an N–H$\cdots$O hydrogen bond involving the amide as the H-bond donor, and one of the oxygen's of the nitro group, O2, as the H-bond acceptor. The short N$\cdots$O distance of 3.1895 (9) Å indicates this interaction to be the strongest individual directional interaction in the lattice of Compound **1**. This interaction is augmented by two C–H$\cdots$O interactions that provide synergy to the single N–H$\cdots$O hydrogen bond. H11, trans to the nitro group on the B ring, interacts with the second nitro oxygen atom, O3, and H2 of the alkene is interacting with the same nitro O atom as the amide. The nitro group thus acts as an acceptor for three hydrogen bonds: one strong N–H$\cdots$O and two weaker C–H$\cdots$O interactions. These interactions connect molecules into H-bonded ribbons that stretch along the c-axis direction (Figure 3). The ribbons are stabilized by another C–H$\cdots$O interaction that involves the amide oxygen as the H-bond acceptor, and H6 of the phenyl ring as the donor.
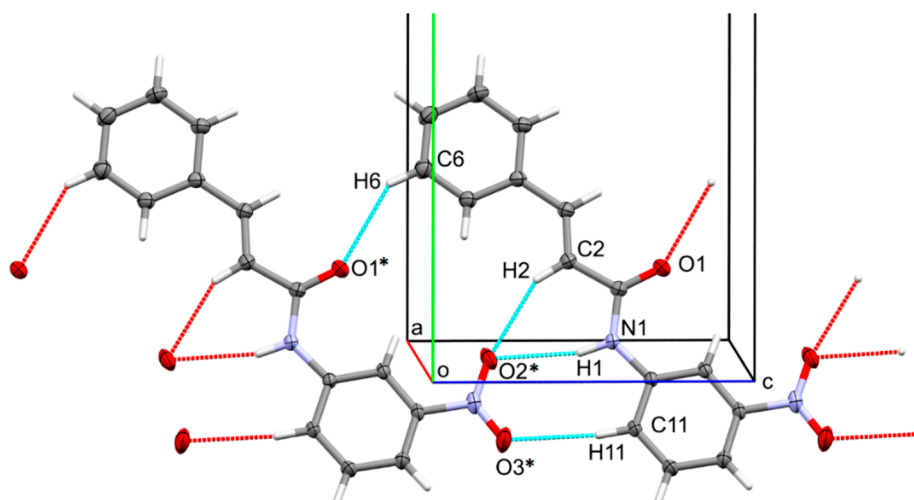
**Figure 3.** N–H···O and C–H···O interactions in Compound **1**, showing a segment of the ribbon of molecules along the c-axis direction. Labels included only for atoms involved in N–H···O and C–H···O interactions (symmetry operator *: x, y, z − 1).

H-bonded ribbons are stacked atop of one another to form π-stacked layers. Individual π-stacking interactions are, however, ill-defined. The shortest centroid to centroid interaction is observed for molecules arranged in head-to-tail parallel pairs, between nitrophenyl and phenyl rings. The centroid distance is, however, as long as 3.9746(6) Å, with slippage between rings of 2.29 Å, indicating a less than ideal π-stacking interaction (Figure 4). Molecules are shifted against each other sideways, and neither the centers of molecules nor the centers of aromatic rings come to rest atop of each other, but their π-systems are in contact with those of several molecules of the parallel ribbon. The shortest individual π-stacking contact involves the amide and nitro units in parallel layers with a $C_{amide}$ to $O_{nitro}$ distance of only 3.1145(11) Å. However, this interaction is not between the same molecule as in the head-to-tail parallel dimers but to the next molecule over (Figure 4). It is thus rather the π-stacking of whole ribbons than that of individual pairs of molecules that provide the driving force for the observed packing arrangement.
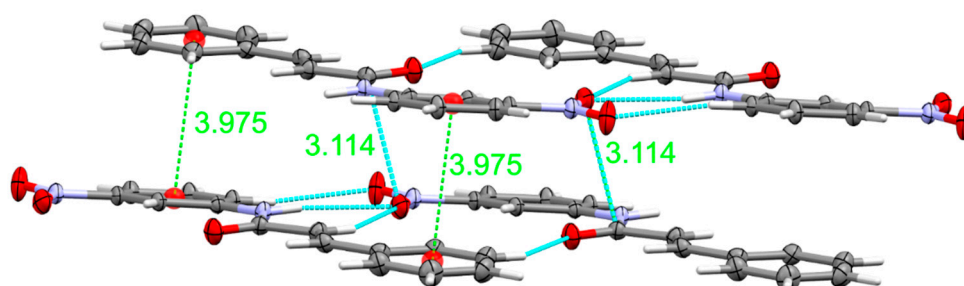


**Figure 4.** Basic π-stacking interactions. Shown are the shortest centroid-to-centroid distances (centroids are shown as red spheres) between phenyl and nitrophenyl rings, and the shortest atom to atom π-stacking interaction between C-amide and O-nitro atoms. Distances in Å.

Ribbons are stacked in both directions, up and down, with slightly different interplanar distances. Depending on the exact definition of planes—molecules in H-bonded ribbons are slightly shifted up or down with respect to each other—interplanar spacing's are between 2.876 and 3.315 Å (other values lie between these two extremes). A representative view of the extended π-stacking is shown in Figure 5. Parallel ribbons are shifted along the planes—mostly along the long unit cell axis (the b-axis).
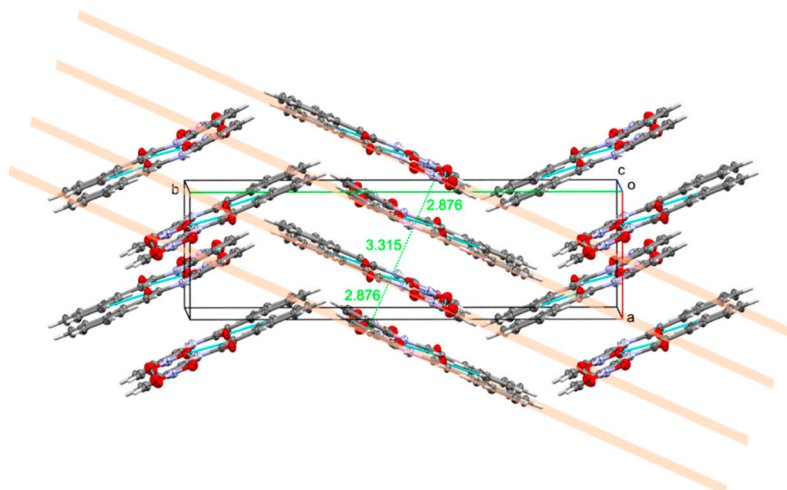
**Figure 5.** Herringbone arrangement of π-stacked ribbons viewed along the c-axis. Parallel planes defined by molecules shown in transparent beige. Interplanar distances are shown in green (Å).

Neighboring stacks of ribbons along the b-axis direction are not coplanar but tilted against each other (Figure 5), at an angle of about 48.11°. Viewed along the c-axis direction, this leads to a herringbone arrangement. No individual directional interactions are found that connect neighboring stacks of ribbons with each other, but phenyl rings slipped away from the stacks and protruding out do interdigitate with their counterparts from the parallel stack, thus creating a zipper-like interaction and preventing stacks from sliding past each other and giving additional stability to the structure overall (Figure 5).

### 3.3. Computational Studies

A plot of the difference in the electron density of the refined structure (Figure 6) shows that most residual electron density is located on bonds between atoms. These results indicate that the spherical atom approach, or atoms in molecules (AIM) approach, for crystal structure refinement, is providing a poor fit of the experimental electron density for Compound **1**. Bonding electrons, or any distortion of electron density from that of a spherical atom other than anisotropic libration, cannot be modeled using a traditional crystal structure refinement against structure factors based on spherical atoms alone. For structures where these deformation densities are making up a large part of the difference in the electron density, a refinement that uses non-spherical structure factors provides an alternative. One such approach is a Hirshfeld Atom Refinement (HAR).

When using HAR, as implemented in Olex2 [12], an improved R-value of 2.23% was observed, as opposed to the Shelxl based AIM model R-value of 4.05%. Specifically, we used HAR with the "Restricted Hartree–Fock" method with the def2-SVP basis set [21,22]. The experimental Shelxl and HAR solid-state geometries for Compound **1** were also compared to DFT calculated gas-phase values. Selected bond distances, bond angles, and torsion angles are given in Table 3. The conformational disagreements amongst the experimental structure (X-ray structure) and optimized equivalents by HAR and the B3LYP functional with 6-311++G(d,p) basis set were determined (Figure 7).

The root-mean-square error (RMSE) of 0.191 Å was obtained on superimposing the optimized (HAR) and X-ray structures of Compound **1**. HAR optimization indicated that the angle of 6.60 (15)° between the planes of the A ring and nitro-substituted B ring of Compound **1**, which is almost similar to the X-ray structures of Compound **1** (6.66 (3)°). The RMSE of 0.204 Å was obtained on superimposing the optimized (B3LYP) and X-ray structures of Compound **1**. The DFT calculations assigned a planar structure to Compound **1** indicated by the angle of 0.153° between the planes of the A ring and nitro-substituted B ring. The optimized structures are relatively planar, while the experimental structure is slightly rotated. The torsion between O1 and H15 twist the molecule slightly, contributing

to the angle of 6.66 (3)° between the planes of the A ring and nitro-substituted B ring. According to our calculations, the significant differences between experimental and calculated bond lengths by HAR and B3LYP were 0.002 Å and 0.009 Å (C2–C3). The significant difference between experimental and calculated bond angles by HAR and B3LYP were 0.2° (C12–C8–N1) and 2.6° (C2–C3–N4), respectively. The discrepancies between experimental and optimized DFT data are not surprising because the B3LYP optimizations were based on the unpacked isolated molecule. Whereas, the packing effects and intermolecular interactions prevail in the solid-state. Even though there are minor differences, calculated geometric parameters represent a good approximation.
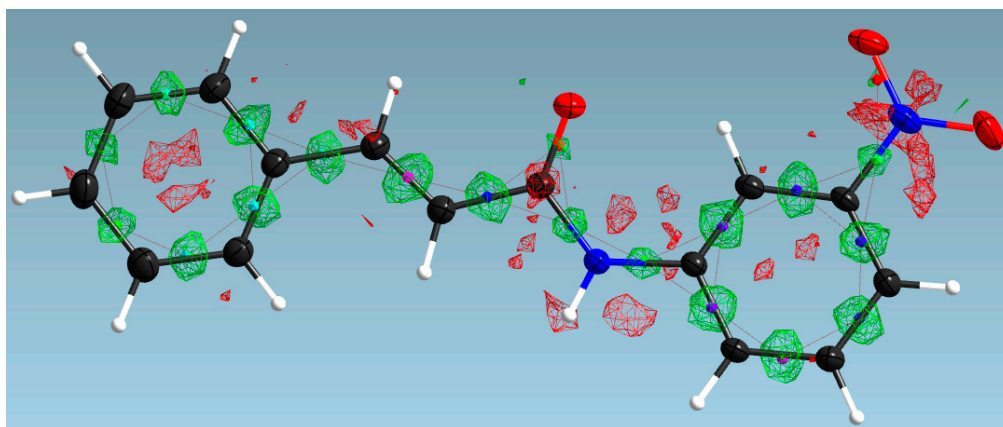


**Figure 6.** $F_{obs}-F_{calc}$ difference electron density plot of the structure refined using the standard anisotropic spherical atom approach (Shelxl2018). The $F_{obs}-F_{calc}$ map cutoff values are at 0.14 electrons per cubic Ångström. Difference densities are located mainly on bond critical points ("bonding electrons").

**Table 3.** Selected bond lengths (Å) and bond angles (°) for Compound **1**.

| Bond Lengths (Å) | | | | Bond Angles (°) | | | |
|---|---|---|---|---|---|---|---|
| A-B | ShelXl | HAR | B3LYP | A-B-A | ShelXl | HAR | B3LYP |
| C1–C2 | 1.479 (11) | 1.480 (6) | 1.483 | O1–C1–N1 | 123.5 (7) | 123.8 (4) | 123.1 |
| C1–N1 | 1.375 (10) | 1.373 (5) | 1.389 | O1–C1–C2 | 124.0 (7) | 123.8 (4) | 123.5 |
| C1–O1 | 1.228 (10) | 1.225 (5) | 1.226 | N1–C1–C2 | 112.5 (7) | 112.5 (3) | 113.4 |
| C2–C3 | 1.337 (11) | 1.339 (6) | 1.346 | C3–C2–C1 | 121.8 (8) | 121.8 (4) | 119.7 |
| C3–C4 | 1.466 (12) | 1.464 (6) | 1.462 | C2–C3–C4 | 125.6 (8) | 125.6 (4) | 128.2 |
| C10–N1 | 1.404 (10) | 1.401 (5) | 1.403 | C1–N1–C10 | 128.3 (7) | 128.0 (3) | 128.8 |
| C14–N2 | 1.465 (10) | 1.463 (5) | 1.477 | C15–C10–N1 | 123.4 (7) | 123.6 (3) | 123.1 |
| N2–O2 | 1.231(10) | 1.225 (5) | 1.229 | C11–C10–N1 | 117.1 (6) | 116.9 (4) | 117.6 |
| N2–O3 | 1.226 (11) | 1.218 (5) | 1.232 | O3–N2–O2 | 123.0 (7) | 122.9 (4) | 124.6 |
| C11–C12 | 1.384 (11) | 1.388 (6) | 1.391 | O3–N2–C14 | 118.4 (7) | 118.4 (4) | 117.5 |
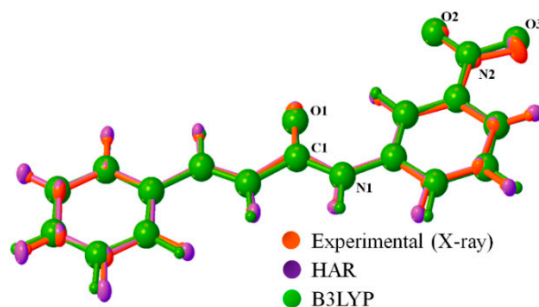


**Figure 7.** Superimposition of the X-ray structure of Compound **1** (orange) and its HAR (purple), B3LYP (green) optimized counterpart (red).

The frontier orbitals were computed using the B3LYP functional and the 6-311++G(d,p) basis set (Figure 8). The HOMO and LUMO of Compound **1** are distributed over the propene amide bridge, phenyl and, nitrophenyl rings. The experimental structure of Compound **1** shows a slight correlation with the reported *p*-nitrophenyl derivative [34]. The reported structure is more planar than Compound **1**, as indicated by a smaller dihedral angle of 3.04 (8)° between the ring A and nitro-substituted ring B.
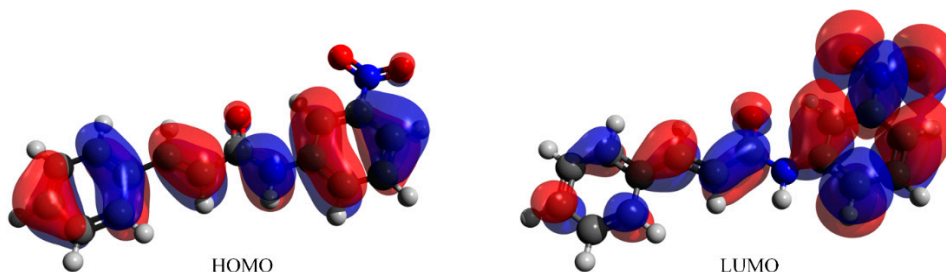


HOMO　　　　　　　　　　　　　　LUMO

**Figure 8.** Frontier orbitals computed using the B3LYP functional and the 6-311++G(d,p) basis set.

Based on the crystallographic data, the π–π stacking interactions provide the largest fraction of the packing interaction energy, leading to the ribbon-like packing arrangement in the crystals. π–π stacking interactions in Compound **1** exceed the hydrogen bonding interactions. This might be contrary to initial perception, as the H-bonding interactions—as strong and directional interactions—are individually having the highest interaction energy. This is, however, more than compensated by the number of atoms involved in the pi-stacking interactions, which exceeds the number of individual H-bonding interactions by order of magnitude. To compute the effect of π–π stacking interactions in the crystals packing arrangement, the UNI forcefield calculations were used [35,36]. The CSD-materials suite in the Mercury program was used to determine the UNI intermolecular potentials for the packing interactions in the solid-state, and the obtained results are presented in Figure 9 (Supplementary Materials Table S1). Compound **1** showed four largest intermolecular interactions that arise from pi-stacking interactions (ranging from −58.5595 to −36.3843 kJ/mol), followed by a pair of (symmetry equivalent) interactions involving the H-bonding interactions within the pi-stacked layers at −24.0213 kJ/mol. These results further contribute to the idea that the π–π stacking interactions are the driving force for this compound to arrange in the ribbons.
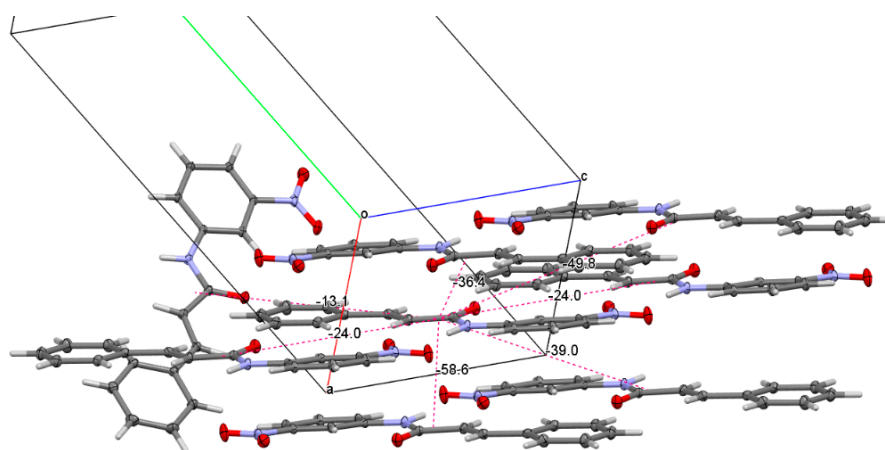


**Figure 9.** Intermolecular potential energies obtained by UNI forcefield calculations.

## 4. Conclusions

*N*-(3-nitrophenyl)cinnamamide was synthesized with the modified method and characterized by NMR, UV-visible and fluorescence spectroscopy, mass spectrometry, and X-ray crystallography. Also, density functional modeling studies, HAR, and the UNI forcefield calculations were reported in

this study. The geometric parameters calculated by using the HAR with the "Restricted Hartree–Fock" method with the def2-SVP basis set and density functional theory (DFT) with the 6–311++G(d,p) basis set are in good agreement with the X-ray structure, despite the observed differences, in general. However, the DFT method allowed us to calculate the bond angles and geometry of the investigated compound with more convenience than HAR refinement. The calculated bond lengths and bond angles showed minor disagreements with the experimental results. The investigated compound was found to crystallize in the monoclinic space group $P2_1$/n with a = 6.7810 (5) Å, b = 23.0913 (15) Å, c = 8.2079 (5) Å, V = 1282.76 (15) Å$^3$, Z = 4. The X-ray single crystallographic study, DFT calculations, and UNI forcefield calculations revealed that packing of molecules in the solid-state is governed by the close to planar and extended conformation of the investigated compound, leading to ribbons of parallel sheets of molecules that are stacked through $\pi-\pi$ stacking interactions. Within each ribbon, molecules are connected through a series of N–H$\cdots$O and C–H$\cdots$O interactions of various strengths.

**Supplementary Materials:** The following are available online at http://www.mdpi.com/2073-4352/9/11/599/s1, Figure S1: $^1$H NMR spectra of compound 1, Figure S2: $^{13}$C NMR spectra of compound 1, Figure S3: Mass spectra of compound 1, UV absorbance spectra of compound 1, Table S1: Calculated inter-molecular potentials energies obtained by UNI forcfield calculations. The supplementary crystallographic data (CCDC 1965718) for the compound 1 can be obtained free of charge from The Cambridge Crystallographic Data Centre via www.ccdc.cam.ac.uk.

**Author Contributions:** S.B.N., S.D.W., and M.Z. wrote the manuscript. J.-S.L. synthesized the compound and obtained the single X-ray quality crystals. S.B.N., J.-S.L., and S.D.W. assisted with compound characterization, including MS and NMR work, and analyzed the data. M.Z. performed the X-ray crystallography experiments. S.B.N. and M.Z. analyzed the X-ray crystallography data. All authors contributed to the revision and final review of the manuscript.

**Conflicts of Interest:** The authors declare that they have no conflict of interest.

## References

1. Hawkey, P.M.; Warren, R.E.; Livermore, D.M.; McNulty, C.A.M.; Enoch, D.A.; Otter, J.A.; Wilson, A.P.R. Treatment of infections caused by multidrug-resistant Gram-negative bacteria: Report of the British Society for Antimicrobial Chemotherapy/Healthcare Infection Society/British Infection Association Joint Working Party. *J. Antimicrob. Chemother.* **2018**, *73*, iii2–iii78. [PubMed]

2. Cornaglia, G. Fighting infections due to multidrug-resistant Gram-positive pathogens. *Clin. Microbiol. Infect.* **2009**, *15*, 209–211. [CrossRef] [PubMed]

3. Lafay, S.; Gil-Izquierdo, A. Bioavailability of phenolic acids. *Phytochem. Rev.* **2008**, *7*, 301–311. [CrossRef]

4. De, P.; Baltas, M.; Bedos-Belval, F. Cinnamic acid derivatives as anticancer agents-a review. *Curr. Med. Chem.* **2011**, *18*, 1672–1703. [CrossRef] [PubMed]

5. Sova, M. Antioxidant and antimicrobial activities of cinnamic acid derivatives. *Mini. Rev. Med. Chem.* **2012**, *2*, 749–767. [CrossRef]

6. Vishnoi, S.; Agrawal, V.; Kasana, V.K. Synthesis and structure-activity relationships of substituted cinnamic acids and amide analogues: A new class of herbicides. *J. Agric. Food. Chem.* **2009**, *57*, 3261–3265. [CrossRef]

7. Olender, D.; Żwawiak, J.; Zaprutko, L. Multidirectional Efficacy of Biologically Active Nitro Compounds Included in Medicines. *Pharmaceuticals* **2018**, *11*, 54. [CrossRef]

8. Ju, K.S.; Parales, R.E. Nitroaromatic compounds; from synthesis to biodegradation. *Microbiol. Mol. Biol. Rev.* **2010**, *74*, 250–272. [CrossRef]

9. El-Hossary, E.M.; Förstner, K.U.; François, P.; Baud, D.; Streker, K.; Schrenzel, J.; Ohlsen, K.; Holzgrabe, U. A Novel Mechanism of Inactivating Antibacterial Nitro Compounds in the Human Pathogen Staphylococcus aureus by Overexpression of a NADH-Dependent Flavin Nitroreductase. *Antimicrob. Agents Chemother.* **2018**, *62*, e01510–e01517. [CrossRef]

10. Nimse, S.B.; Pal, D.; Mazumder, A.; Mazumder, R. Synthesis of Cinnamanilide Derivatives and Their Antioxidant and Antimicrobial Activity. *J. Chem.* **2015**, *2015*, 1–5. [CrossRef]

11. Krause, L.; Herbst-Irmer, R.; Sheldrick, G.M.; Stalke, D. Comparison of silver and molybdenum microfocus X-ray sources for single-crystal structure determination. *J. Appl. Cryst.* **2015**, *48*, 3–10. [CrossRef] [PubMed]

12. *SHELXTL Suite of Programs*, version 6.14; Bruker Advanced X-ray Solutions, Bruker AXS Inc.: Madison, WI, USA, 2003.

13. Sheldrick, G.M. A short history of SHELX. *Acta Cryst. A* **2008**, *64*, 112–122. [CrossRef] [PubMed]

14. Sheldrick, G.M. Crystal structure refinement with SHELXL. *Acta Cryst.* **2015**, *C71*, 3–8.

15. Hübschle, C.B.; Sheldrick, G.M.; Dittrich, B. ShelXle: A Qt graphical user interface for SHELXL. *J. Appl. Crystallogr.* **2011**, *44*, 1281–1284. [CrossRef] [PubMed]

16. Dolomanov, O.V.; Bourhis, L.J.; Gildea, R.J.; Howard, J.A.K.; Puschmann, H. OLEX2: A complete structure solution; refinement and analysis program. *J. Appl. Crystallogr.* **2009**, *42*, 339–341. [CrossRef]

17. Macrae, C.F.; Edgington, P.R.; McCabe, P.; Pidcock, E.; Shields, G.P.; Taylor, R.; Towler, M.; van de Streek, J. Mercury: Visualization and analysis of crystal structures. *J. Appl. Crystallogr.* **2006**, *39*, 453–457. [CrossRef]

18. Macrae, C.F.; Bruno, I.J.; Chisholm, J.A.; Edgington, P.R.; McCabe, P.; Pidcock, E.; Rodriguez-Monge, L.; Taylor, R.; van de Streek, J.; Wood, P.A. Mercury CSD 2.0—New features for the visualization and investigation of crystal structures. *J. Appl. Crystallogr.* **2008**, *41*, 466–470. [CrossRef]

19. Spek, A.L. Single-crystal structure validation with the program PLATON. *J. Appl. Cryst.* **2003**, *36*, 7–13. [CrossRef]

20. *The PyMOL Molecular Graphics System, version 1.3r*; Schrödinger LLC: New York, NY, USA, 2010.

21. Cason, C.; Frolich, T.; Lipka, C. *POV-Ray—The Persistence of Vision Raytracer. 3.7.0 edn*, 2013.

22. Weigend, F.; Ahlrichs, R. Balanced basis sets of split valence; triple zeta valence and quadruple zeta valence quality for H to Rn: Design and assessment of accuracy. *Phys. Chem. Chem. Phys.* **2005**, *7*, 3297–3305. [CrossRef]

23. Schuchardt, K.L.; Didier, B.T.; Elsethagen, T.; Sun, L.; Gurumoorthi, V.; Chase, J.; Li, J.; Windus, T.L. Basis set exchange: A community database for computational sciences. *J. Chem. Inf. Model.* **2007**, *47*, 1045–1052. [CrossRef]

24. Frisch, M.J.; Trucks, G.W.; Schlegel, H.B.; Scuseria, G.E.; Robb, M.A.; Cheeseman, J.R.; Montgomery, J.A.; Vreven, T.; Kadin, K.N.; Burant, J.C.; et al. *Gaussian 03*; revision B03; Gaussian Inc.: Pittsburgh, PA, USA, 2003.

25. Hariharan, P.C.; Pople, J.A. Accuracy of $AH_n$ equilibrium geometries by single determinant molecular orbital theory. *Mol. Phys.* **2006**, *27*, 209–214. [CrossRef]

26. Kohn, W.; Becke, A.D.; Parr, R.G. Density Functional Theory of Electronic Structure. *J. Phys. Chem.* **1996**, *100*, 12974–12980. [CrossRef]

27. Hanwell, M.D.; Curtis, D.E.; Lonie, D.C.; Vandermeersch, T.; Zurek, E.; Hutchison, G.R. Avogadro: An advanced semantic chemical editor, visualization, and analysis platform. *J. Cheminfo.* **2012**, *4*, 17. [CrossRef] [PubMed]

28. Lee, W.W.; Tong, G.L.; Martinez, A.P.; Weinstein, B.; Schelstraete, M.G.; Baker, B.R.; Goodman, L. Synthesis of N,N-bis(2-chloroethyl)-DL-phenylalanine hydrochloride. *J. Med. Chem.* **1963**, *6*, 439–442. [CrossRef]

29. Alberghina, G.; Arcoria, A.; Fisichella, S. Reaction kinetics of cinnamoyl, β-2-furylacryloyl, and β-2-thienylacryloyl chlorides with anilines in benzene. *J. Org. Chem.* **1978**, *43*, 1122–1125. [CrossRef]

30. Kim, T.H.; Huh, C.; Lee, B.S.; Lee, I. Nucleophilic substitution reactions of cinnamoyl chlorides with anilines in acetonitrile and acetonitrile-methanol mixtures. *J. Chem. Soc. Perkin Trans 2* **1995**, *12*, 2257–2261. [CrossRef]

31. Yamada, A.; Tomishima, M.; Hayashida, H.; Imanishi, M.; Spears, G.W.; Ito, K.; Takahashi, F.; Miyake, H. Novel Amide Compounds. European Patent EP 1 264 820 A1, 11 December 2002.

32. Chute, J.P.; Jung, M.E.; Diers, E. Compounds and Methods for Hematopoietic Regeneration. World Intellectual Property. Organization Patent WO 2019/108800 A1, 6 June 2019.

33. Wang, T.C.; Chen, Y.L.; Lee, K.H.; Tzeng, C.C. Lewis Acid Catalyzed Reaction of Cinnamanilides: Competition of Intramolecular and Intermolecular Friedel–Crafts Reaction. *Synthesis* **1997**, *1997*, 87–90. [CrossRef]

34. Saeed, A.; Khera, R.A.; Shahidb, M.; Parvez, M. N-(4-Nitrophenyl)cinnamamide. *Acta. Cryst. Sect. E Struct.* **2009**, *E65*, o2068. [CrossRef]

35. Gavezzotti, A. Are Crystal Structures Predictable? *Acc. Chem. Res.* **1994**, *27*, 309–314. [CrossRef]

36. Gavezzotti, A.; Filippini, G. Geometry of the Intermolecular X-H···Y (X, Y = N, O) Hydrogen Bond and the Calibration of Empirical Hydrogen-Bond Potentials. *J. Phys. Chem.* **1994**, *98*, 4831–4837. [CrossRef]